Article

Not peer-reviewed version

Enhanced Photocatalytic Antibacterial Property by Regulating the Built-in Electric Field of BiVO4 with a Piezoelectric Mineral Tourmaline

Nina Zhan , Jia Geng , Peter Jiang , Alison Wang , Yue Yu , Fengkai Yu , Zhen Yang *

Posted Date: 22 October 2025

doi: 10.20944/preprints202510.1766.v1

Keywords: photocatalytic antibacterial; built-in electric field enhancement; Tourmaline/BiVO4; spontaneous polarization

 doi:10.20944/preprints202510.1766.v1

Article

Enhanced Photocatalytic Antibacterial Property by Regulating the Built-in Electric Field of $BiVO_4$ with a Piezoelectric Mineral Tourmaline

Nina Zhan [1], Jia Geng [1], Peter Jiang [1], Alison Wang [1], Yue Yu [2], Fengkai Yu [3] and Zhen Yang [1,*]

[1] YM American Academy, 502 Wake Forest Dr., Newark, DE 19713, USA

[2] College of Arts and Sciences, The Ohio State University, 164 Annie & John Glenn Ave., Columbus, Ohio 43210, USA

[3] Institute of Green Chemistry and Industrial Catalysis, School of Chemistry and Chemical Engineering, Qingdao University, Qingdao 266071, China

* Correspondence: ztyang@ymamerican.com; Tel.: +1(302)257-1537

Abstract

Photocatalytic antimicrobial materials represent a promising class of sustainable disinfection technologies, leveraging the generation of reactive oxygen species (ROS) under light irradiation for environmental and biomedical applications. Bismuth vanadate ($BiVO_4$), a visible-light-responsive semiconductor, has garnered considerable interest due to its suitable bandgap and chemical stability. However, its photocatalytic performance is critically limited by rapid charge carrier recombination and a relatively weak intrinsic built-in electric field. In this study, we report a novel composite strategy to address these limitations by coupling $BiVO_4$ with tourmaline, a naturally abundant piezoelectric mineral exhibiting spontaneous polarization. The integration of tourmaline induces a built-in electric field that synergistically aligns with and amplifies the internal field of $BiVO_4$, which substantially improves charge separation and carrier transport dynamics. The resulting tourmaline/$BiVO_4$ heterostructure demonstrates remarkedly enhanced antibacterial activity under visible-light irradiation against both *Escherichia coli* and *Staphylococcus aureus*, significantly outperforming pristine $BiVO_4$. Mechanistic investigations attribute this enhancement to the polarization-induced modulation of interfacial charge dynamics, which boosts ROS generation and accelerates microbial inactivation kinetics. This work presents a generalizable strategy for the rational design of high-efficiency photocatalytic antimicrobial systems, offering potential utility in water treatment, healthcare sterilization, and environmental remediation.

Keywords: photocatalytic antibacterial; built-in electric field enhancement; Tourmaline/$BiVO_4$; spontaneous polarization

1. Introduction

Infectious diseases instigated by pathogenic bacteria continue to pose a pervasive threat to global public health, exacerbated by the emergence and proliferation of multidrug-resistant (MDR) strains that undermine the effectiveness of conventional antimicrobial therapies. Infectious diseases driven by pathogenic bacteria remain a critical global health challenge, exacerbated by their pervasive presence in both clinical settings and the environment. Among these challenges, the microbial contamination of water sources resulting from anthropogenic activities, such as agricultural runoff, sewage discharge, and industrial effluents, poses a critical barrier to ensuring safe drinking water. Pathogenic bacteria, such as *Escherichia coli*, *Salmonella spp.*, and *Vibrio cholerae*, are frequently implicated in waterborne disease outbreaks, contaminating both surface and groundwater systems on an alarming scale [1]. Conventional disinfection strategies, notably chlorination and ozonation, remain cornerstones of municipal water treatment infrastructure. However, their efficacy is

 doi:10.20944/preprints202510.1766.v1

increasingly constrained by several physicochemical and microbiological factors, particularly in the inactivation of chlorine- and ozone-resistant strains. Chlorination, albeit effective against a broad spectrum of pathogens, is associated with the generation of disinfection byproducts (DBPs) such as trihalomethanes (THMs) and haloacetic acids (HAAs), which are persistent and linked to carcinogenic outcomes in humans [2]. Ozonation, though a potent oxidizing method, suffers from inherent limitations, including ozone's rapid decomposition, necessitating on-site generation and continuous replenishment to sustain disinfection potency [3]. Moreover, both chlorine-based agents and ozone can produce secondary pollutants or residual toxicity, raising ecological and toxicological concerns. Notably, failures in disinfection protocols, such as suboptimal chlorine dosing, have contributed to significant public health incidents. This includes multistate outbreaks of Salmonella, underscoring the urgent necessity for next-generation antimicrobial technologies that are both broad-spectrum and environmentally benign.

Therefore, the development of high-efficiency photocatalytic antibacterial materials is of paramount importance for advancing global health and environmental resilience, directly contributing to the realization of the United Nations Sustainable Development Goals (SDGs), particularly SDG 3 (Good Health and Well-being) and SDG 6 (Clean Water and Sanitation). Over recent decades, photocatalytic antimicrobial technologies have experienced significant growth, with demonstrated applicability across a broad range of sectors including healthcare disinfection [4], water purification [5], and environmental remediation [6]. These materials harness solar irradiation to generate reactive species that effectively inactivate pathogenic microorganisms, thereby offering a sustainable, non-toxic, and energy-efficient route to mitigating microbial contamination [7]. As such, the rational design and advancement of visible-light-responsive photocatalysts represent a critical frontier in safeguarding public and environmental health. Therefore, advancing visible-light-responsive photocatalysts represents a critical strategy for mitigating bacterial threats and safeguarding environmental and human health. Traditionally, research in this domain has been predominantly centered on titanium dioxide (TiO_2), a benchmark photocatalyst known for its chemical stability and photocatalytic efficacy under ultraviolet (UV) light. However, TiO_2 is limited by its wide band gap (~3.2 eV), rendering it only photoactive under UV irradiation, which comprises merely ~4% of the solar spectrum [8]. This limitation has prompted a strategic shift toward the exploration of alternative photocatalysts that can efficiently harvest visible light, which accounts for approximately 45% of solar energy. Among these, bismuth vanadate ($BiVO_4$) has emerged as a particularly attractive candidate due to its narrow band gap (~2.4 eV), high chemical stability, non-toxicity, and resistance to photocorrosion [8].

$BiVO_4$ exists in three principal crystalline polymorphs: tetragonal zircon, tetragonal scheelite, and monoclinic scheelite [9]. The tetragonal zircon phase features valence and conduction bands primarily derived from O 2p and V 3d orbitals, whereas the scheelite-type structures incorporate Bi 6s and O 2p orbital contributions into the valence band, leading to a reduction in band gap energy [10]. Specifically, the monoclinic scheelite phase demonstrates superior photocatalytic performance, attributed to its enhanced charge separation and broader visible-light absorption [11]. The intrinsic band gap of $BiVO_4$ (~2.42 eV) enables efficient harvesting of the visible spectrum, while its crystal structure and optical properties further support its candidacy as a solar-driven photocatalyst [9].

Despite these advantages, $BiVO_4$ suffers from diminished photocatalytic efficacy relative to isostructural semiconductor materials, attributed to suboptimal charge carrier mobility, elevated recombination kinetics, and inefficient interfacial charge transfer mechanisms [12]. Additionally, $BiVO_4$ suffers from a low conduction band potential and fast recombination of photoinduced electron-hole pairs. In aqueous environments, $BiVO_4$ often forms microcrystalline aggregates with low surface area and smooth facets, leading to suboptimal dispersion and reduced photocatalytic contact with target contaminants [13]. These drawbacks necessitate innovative material design strategies, such as heterojunction formation, surface modification, or internal field engineering, to overcome the kinetic barriers of $BiVO_4$.

 doi:10.20944/preprints202510.1766.v1

One of the principal limitations governing the suboptimal photocatalytic performance of $BiVO_4$ is its inherently low electronic conductivity, which significantly impedes efficient charge carrier transport. This poor conductivity restricts the migration of photogenerated electrons and holes to active surface sites, thereby increasing the likelihood of bulk recombination events and reducing the quantum efficiency of photocatalytic processes. The electronic structure of $BiVO_4$ plays a pivotal role in mediating this recombination behavior. For instance, doping studies involving molybdenum (Mo) and tungsten (W) have demonstrated that strategic elemental substitution not only enhances electrical conductivity but also suppresses recombination rates by over an order of magnitude. This is primarily attributed to the modulation of the conduction band edge, which remains energetically lower than the reduction potential required for superoxide radical anion ($\cdot O_2^-$) formation, a critical reactive species in oxidative photocatalysis. Consequently, photogenerated electrons often lack the thermodynamic driving force to initiate redox reactions before undergoing recombination, thereby diminishing photocatalytic efficacy. The conduction band's relatively low energy level plays a role in reducing the stability of photogenerated electrons. Moreover, the band structure of $BiVO_4$ across both its monoclinic scheelite and tetragonal zircon polymorphs governs the charge separation and recombination processes. The relatively low conduction band minimum (CBM) compromises the stability and reactivity of photoexcited electrons, further exacerbating recombination kinetics [14].

In this context, the integration of piezoelectric materials offers a compelling strategy for facilitating spatially resolved charge separation. The piezoelectric effect, activated under mechanical stimuli such as compressive strain, ultrasonic vibration, or external mechanical deformation, generates an internal electric field via ferroelectric polarization. This strain-induced piezoelectric potential induces directional migration of photogenerated charge carriers, establishing a built-in electric field that serves to spatially separate electrons and holes. The resultant band bending at the interface generates a favorable thermodynamic gradient, promoting carrier diffusion, effectively elongating their diffusion lengths and enhancing carrier lifetimes. This field induces directional migration of photogenerated electrons and holes via strain-induced piezoelectric potential, thereby minimizing recombination kinetics [15]. This piezoelectric modulation has been widely leveraged in functional optoelectronic systems, including photocatalytic water splitting, CO_2 photoreduction, and environmental pollutant degradation, where efficient charge utilization is critical [16].

Since tourmaline is a naturally abundant mineral and can be utilized with minimal post-processing, its implementation as a functional material aligns with principles of environmental sustainability. Functionally analogous to magnetic dipoles, tourmaline crystals exhibit spontaneous polarization, enabling their use as naturally occurring electrodes in energy conversion systems. Among piezoelectric minerals, tourmaline demonstrates one of the highest piezoelectric coefficients, with a reported value of 4.1 pC/N, resulting in a substantial charge output of 4.1×10^{-9} C and a voltage of 0.41 V under an applied force of 1000 N. This performance surpasses that of other naturally piezoelectric materials such as quartz, topaz, and zinc-based compounds, which are limited either by lower conversion efficiency or by material instability under operating conditions. Under external mechanical stimuli, such as vibration, seismic motion, or compressive force, tourmaline undergoes polarization-induced potential generation. This charge separation can be harnessed via electrodes to produce usable electrical energy, rendering it a promising eco-compatible component for hybrid piezo-photocatalytic system [17].

2. Materials and Methods

2.1. Chemicals and Reagents

Tourmaline powder (10,000 mesh; Hebei, China), bismuth nitrate pentahydrate ($Bi(NO_3)_3{\cdot}5H_2O$, AR), ammonium metavanadate (NH_4VO_3, AR), citric acid monohydrate ($C_6H_8O_7{\cdot}H_2O$, AR), ammonia solution ($NH_3{\cdot}H_2O$, 25 wt.%, AR), and deionized water were used throughout the study. All reagents were of analytical grade and used as received without further purification.

 doi:10.20944/preprints202510.1766.v1

2.2. Synthesis of Tourmaline/$BiVO_4$ Composite Materials

Tourmaline powder was pre-treated to enhance its surface polarity. Specifically, the powder was dispersed in a 1 M HCl aqueous solution and subjected to ultrasonic treatment for 30 minutes. The resulting suspension was repeatedly washed with deionized water until a neutral pH was achieved, followed by drying at 60 °C in air for 6 hours [18].

The Tourmaline/$BiVO_4$ composite materials were synthesized via a modified sol–gel method. First, 0.01 mol of $Bi(NO_3)_3 \cdot 5H_2O$ and 0.02 mol of citric acid monohydrate were dissolved in 50 mL of 2.0 mol·L^{-1} HNO_3 under constant magnetic stirring to form solution A. Simultaneously, 0.01 mol of NH_4VO_3 and 0.02 mol of citric acid monohydrate were dissolved in deionized water to obtain solution B. Solution A was then added dropwise to solution B under continuous stirring to yield solution C. Pre-treated tourmaline powder was subsequently added to solution C at various mass ratios. The pH of the suspension was adjusted to 7.0 using 25 wt.% ammonia solution, and the mixture was maintained at 80 °C in a water bath with constant stirring until a gelatinous precursor formed. This precursor was thermally treated at 550 °C for 4 hours in air. After natural cooling to room temperature, the resulting yellow powders were collected.

Composites with various tourmaline loadings were synthesized using similar procedure and labeled as 2 wt.%, 6 wt.%, and 10 wt.% Tourmaline/$BiVO_4$, corresponding to the respective mass ratios.

2.3. Characterization

The crystalline phase compositions of the synthesized samples were analyzed via X-ray diffraction (XRD) using a DX-2700 diffractometer (Dandong Haoyuan, China) equipped with Cu Kα radiation (λ = 0.15418 nm), operating over a 2θ range of 5°–60°. Surface morphology and microstructural features were examined using scanning electron microscopy (SEM) on a JSM-6390F instrument (JEOL, Tokyo, Japan) at an accelerating voltage of 20.0 kV. Optical absorption characteristics were analyzed using UV–Vis diffuse reflectance spectroscopy (DRS) on a Hitachi U3900H spectrophotometer (Hitachi, Japan), with band gap energies estimated from *Tauc* plots. Photoluminescence (PL) spectra were recorded using a Hitachi F-4600 spectrophotometer under excitation from a continuous Xe lamp (λ = 325 nm, 150 mW) to evaluate charge carrier recombination behavior.

The local bonding environments and vibrational modes of the composites were further investigated via Raman spectroscopy and Fourier-transform infrared (FTIR) spectroscopy. Raman measurements were performed using a Thermo DXR Raman microscope system (Thermo Fisher Scientific, USA) equipped with a 532 nm laser source, collecting spectra in the 100–1200 cm^{-1} range. FTIR analysis was conducted using a Nicolet iS50 spectrometer (Thermo Fisher Scientific, USA) to assess functional group interactions and confirm the presence of constituent phases.

2.4. Photocatalytic Performance Investigation

The photocatalytic antibacterial performance of the synthesized composites was evaluated by measuring the inactivation efficiency of representative bacterial strains. Antibacterial assays were performed under visible-light irradiation to simulate practical environmental conditions. An 800 W xenon lamp equipped with a 420 nm cutoff filter served as the visible-light source. *Escherichia coli* (Gram-negative) and *Staphylococcus aureus* (Gram-positive) were selected as model bacterial species for photocatalytic disinfection studies [19]. Bacterial stock suspensions were prepared with concentrations of 10⁸–10⁸colony-forming units per milliliter (cfu/mL).

In each experiment, 50 mg of the photocatalyst was dispersed in 49.5 mL of sterilized natural seawater, followed by the addition of 500 μL of bacterial suspension. The resulting mixture was transferred into 50 mL quartz tubes. Before illumination, the suspension was stirred magnetically in the dark for 60 minutes to establish adsorption–desorption equilibrium between the bacterial cells and photocatalyst surface. Subsequent visible-light irradiation was carried out under continuous

 doi:10.20944/preprints202510.1766.v1

stirring. At hourly intervals over a 3-hour exposure period, 1 mL aliquots were extracted, serially diluted using sterile seawater, and plated (100 μL per plate) on Luria–Bertani (LB) agar under aseptic conditions [19]. The inoculated plates were incubated at 37 °C for 18 hours, after which the number of viable bacterial colonies (cfu) was enumerated. The photocatalytic antibacterial efficiency was calculated using the following equations:

$$Survival\ rate\ (\%) = (\frac{N_t}{N_0}) \times 100 \qquad (1)$$

$$Antimicrobial\ rate\ (\%) = 100 - Survival\ rate \qquad (2)$$

Where, N_0 and N_t denote the number of bacterial colonies in the control (absence of photocatalyst) and in the photocatalyst-treated sample at time t, respectively.

Moreover, photoelectrochemical (PEC) measurements were conducted to evaluate the photo-to-current conversion efficiency, charge transfer kinetics, and structural-electronic variations of the photocatalytic materials under visible-light irradiation. A conventional three-electrode configuration was employed, comprising a $BiVO_4$-based working electrode, an Ag/AgCl reference electrode (saturated in 3.0 mol·L^{-1} KCl), and a platinum foil serving as the counter electrode. The measurements were performed using a CompactStat.h10800 electrochemical workstation (Ivium Technologies). Photocurrent response curves were recorded under visible-light illumination using a 300 W xenon lamp equipped with a 420 nm cutoff filter ($\lambda \geq 420$ nm) to exclude UV radiation. Aqueous solutions of 1 mol·L^{-1} Na_2SO_4 and Na_2SO_3 were employed as the electrolyte media in all electrochemical experiments to ensure ionic conductivity and minimize interfacial resistances.

3. Results

3.1. Structural and Morphological Analysis

Figure 1 presents the X-ray diffraction (XRD) patterns of the synthesized samples. All materials exhibit sharp and well-defined diffraction peaks, indicative of high crystallinity. The reference pattern for pure monoclinic $BiVO_4$ (denoted as BVO) corresponds to the standard data from JCPDS card No. 83-1699. Characteristic diffraction peaks are observed at 2θ values of approximately 18.9°, 28.9°, 30.5°, 34.5°, and 35.2°, which are indexed to the (011), (112), (004), (200), and (020) planes, respectively, which align to the characteristic peaks of monoclinic scheelite BVO [20]. This result indicated that the incorporation of tourmaline does not alter the monoclinic crystal structure of $BiVO_4$. However, despite similar diffraction peaks, a subtle rightward shift in the diffraction peaks of tourmaline-containing composites toward higher 2θ values is observed. This shift implies a reduction in the interplanar spacing d, suggesting lattice compression or interfacial strain effects induced by the interaction between $BiVO_4$ and tourmaline. According to Bragg's Law [21]:

$$2dsin\theta = n\lambda \qquad (3)$$

Where, d is the interplanar spacing, λ is the wavelength, and n is the number of reflection stages.

 doi:10.20944/preprints202510.1766.v1

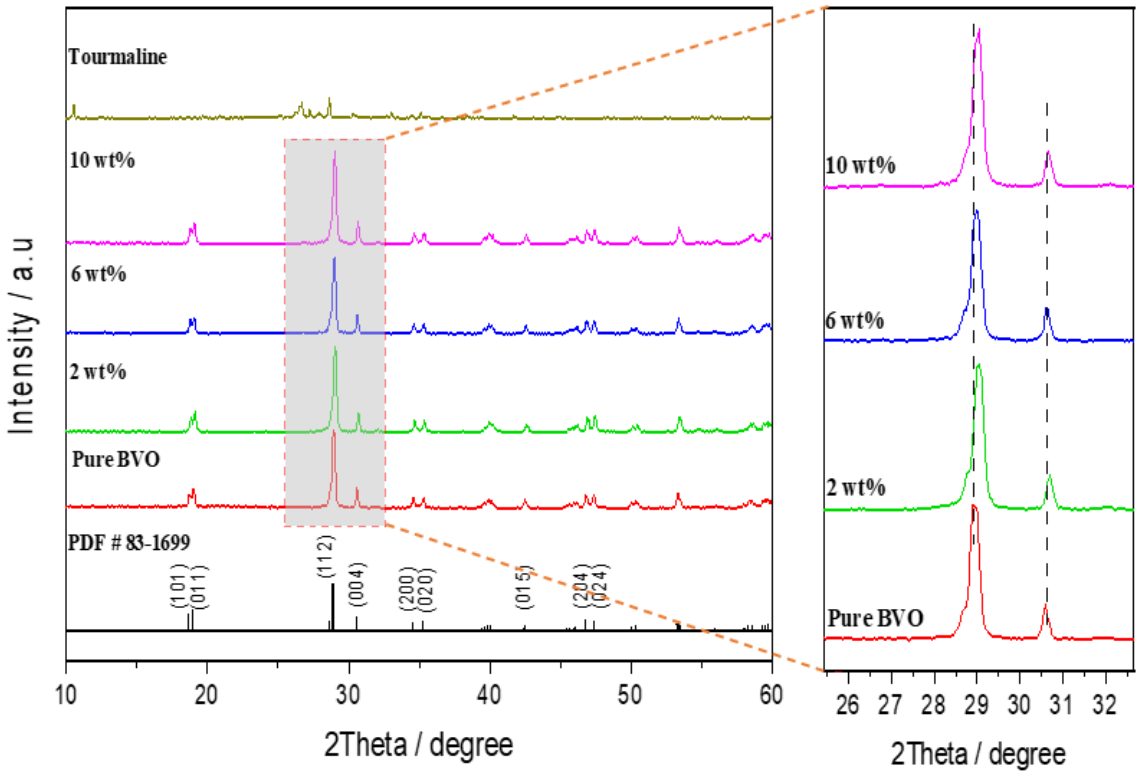

Figure 1. (a) XRD patterns of as-synthesized samples: Pure BVO, n wt.% Tourmaline/BVO.

It is also noteworthy that no distinct diffraction peaks attributable to tourmaline are detected in the composite patterns, likely due to its low mass fraction or its amorphous distribution within the $BiVO_4$ matrix.

Scanning electron microscopy (SEM) was employed to further investigate the morphology and microstructure of the as-prepared materials. Figure 2a–d displays representative SEM images of pristine tourmaline powder, pure $BiVO_4$, and $BiVO_4$ composites containing 6 wt.% and 10 wt.% tourmaline. The untreated tourmaline powder exhibits an irregular, bulk-like morphology with no defined particle shape. In contrast, $BiVO_4$ synthesized via the sol–gel method forms relatively uniform spherical particles with an average size of ~800 nm. For the 6 wt.% and 10 wt.%Tourmaline/$BiVO_4$ composites, $BiVO_4$ nanoparticles are observed to be uniformly anchored on the tourmaline surface, suggesting effective dispersion and strong interfacial contact. This well-distributed structure likely facilitates the enhanced charge separation and interfacial transport critical for improved photocatalytic activity.

 doi:10.20944/preprints202510.1766.v1

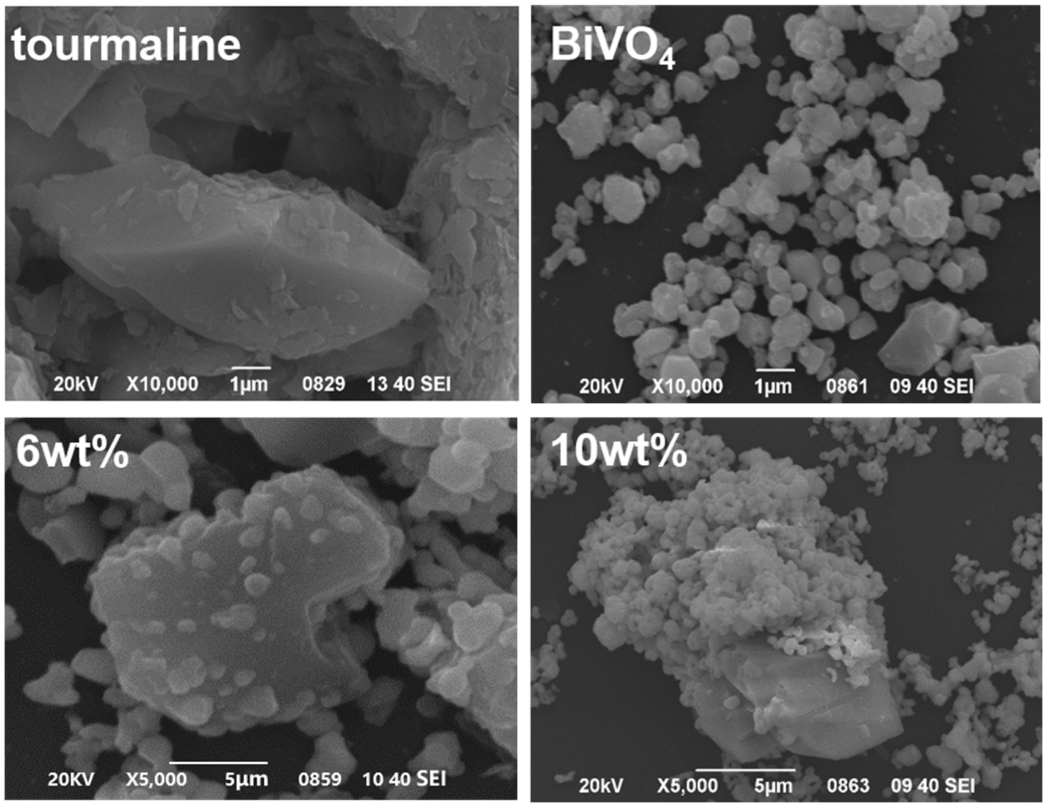

Figure 2. (a) Images of Scanning electron microscopy for as-synthesized samples: Pure tourmaline, Pure BVO, 6 wt.% Tourmaline/BVO and 10 wt.% Tourmaline/BVO.

3.2. The Local Structure of the Composite Photocatalysts

Raman spectroscopy and infrared (IR) reflectance spectroscopy were employed to investigate the local structural and vibrational properties of the synthesized samples. Raman spectroscopy is based on the inelastic scattering of monochromatic light, where energy exchange between incident photons and vibrational or phonon modes results in a wavelength shift. Raman-active modes correspond to vibrations that induce a change in the polarizability tensor of the molecule or lattice [18]. Infrared Reflectance Spectroscopy (often meaning mid-IR reflectance or FTIR in reflectance mode) probes vibrational transitions via absorption (and consequent changes in reflectance) of IR radiation; IR-active modes are those that involve a change in the dipole moment during vibration. Together, these techniques offer complementary insights into lattice dynamics, crystallographic orientation, and local symmetry [22].

Figure 3 displays the Raman spectra of $BiVO_4$ powders with various tourmaline mass ratios, measured in the spectral range of 100–1100 cm^{-1}. Several characteristic vibrational modes associated with the VO_4^{3-} tetrahedron are evident. The bands near 324 and 366 cm^{-1} are attributed to symmetric and asymmetric bending vibrations, respectively [23], while the prominent peak at 640 cm^{-1} corresponds to the asymmetric stretching of the shorter V–O bonds. Peaks around 710 and 811 cm^{-1} are assigned to symmetric stretching modes, which provide further insight into V–O bond lengths [24]. Moreover, external lattice modes such as translational and rotational motions are observed near 213 cm^{-1}. Pure tourmaline exhibited no detectable Raman activity within this spectral window, consistent with its complex silicate structure and low Raman cross-section. However, with increasing tourmaline content in the $BiVO_4$ matrix, notable shifts in Raman band positions and intensities were observed. Specifically, the asymmetric deformation mode (~366 cm^{-1}) shifted toward higher wavenumbers, while the symmetric deformation mode (~324 cm^{-1}) shifted to lower wavenumbers as the mass ratio of tourmaline increased. These spectral shifts suggest structural distortion and symmetry breaking in the VO_4^{3-} tetrahedral units, likely induced by internal electric fields generated by the spontaneously polarized tourmaline. Such distortions indicate lattice strain and modified local

 doi:10.20944/preprints202510.1766.v1

symmetry environments, which can significantly influence the electronic structure and carrier dynamics of the material. The observed changes are consistent with enhanced electron–hole separation and improved photocatalytic performance discussed in subsequent sections. Overall, the Raman analysis reveals that tourmaline integration alters the vibrational characteristics of $BiVO_4$, confirming strong interfacial interaction and lattice modulation within the composite.

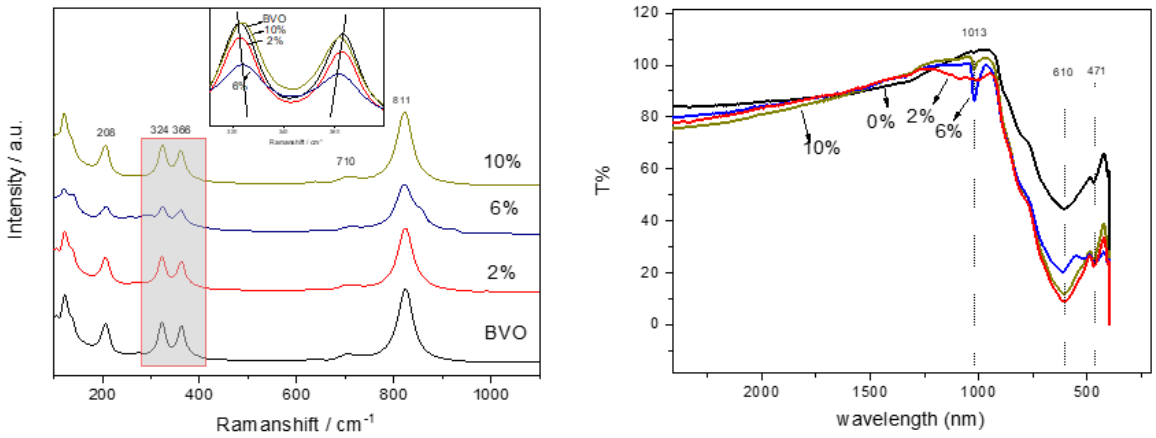

Figure 3. (a) Raman and (b) FTIR spectroscopy of as-synthesized samples: Pure BVO, n wt.% Tourmaline/BVO.

To further elucidate the molecular vibrations and bonding environment within the tourmaline/$BiVO_4$ composite, Fourier-transform infrared spectroscopy in attenuated total reflectance mode (FT-ATR-IR) was employed (FT-ATR-IR) [25]. As shown in Figure 4, the characteristic vibrational bands of $BiVO_4$ were observed, including the V–O stretching vibration at 610 cm^{-1} and the Bi–O bending mode at 471 cm^{-1} [26]. These results confirm the retention of the $BiVO_4$ crystal structure, particularly its photocatalytically favorable monoclinic phase.

A prominent peak at ~1050 cm^{-1}, corresponding to the Si–O stretching vibration, was also detected [27], indicating the presence of tourmaline, whose silicate framework includes Si–O bonds as a structural motif. As observed, the intensity and sharpness of this peak increased with the tourmaline mass ratio, suggesting enhanced structural integration and higher degrees of crystallinity within the composite. Ultimately, these observations imply that the incorporation of tourmaline contributes to a more ordered and uniform bonding environment, possibly enhancing charge separation and stability. Collectively, the FT-IR results confirm successful compounding of tourmaline into the $BiVO_4$ matrix and suggest that increasing tourmaline content induces improved structural organization, which could positively influence the photocatalytic behavior of the material.

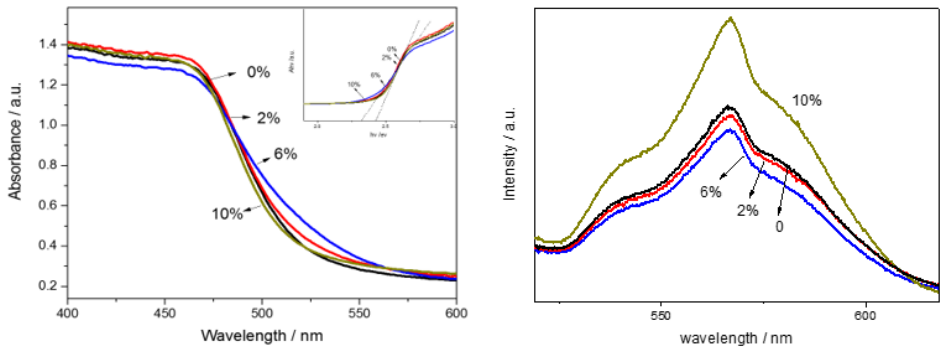

Figure 4. (a) UV-Vis DRS (inset Tauc plots), **(b)** and **(c)** PL spectra of as-synthesized samples: Pure BVO, n wt.% Tourmaline/BVO. **(d)** Schematic illustration of band structure over BVO and 2%Tourmaline/BVO.

 doi:10.20944/preprints202510.1766.v1

3.3. The Photophysical Property of the Photocatalysts

UV–Visible diffuse reflectance spectroscopy (UV–Vis DRS) was conducted to evaluate the optical absorption behavior of the composite materials. This technique is particularly suited for assessing the band structure and light-harvesting capability of semiconductor photocatalysts. As shown in Figure 5, all samples exhibited strong absorption in the visible light region (400–700 nm). Pristine $BiVO_4$, known as a visible-light-responsive semiconductor, exhibits a narrow band gap (~2.4–2.5 eV), enabling absorption up to approximately 520 nm. This visible-light activity arises from electronic transitions from the valence band (dominated by O 2p orbitals) to the conduction band (primarily V 3d orbitals). The composite samples maintained a steep absorption edge, indicating that the visible-light absorption is primarily due to intrinsic band-to-band transitions, rather than sub-bandgap transitions via defect states or impurity levels. This behavior is characteristic of a well-crystallized semiconductor with either a direct or indirect allowed transition, depending on the phase (e.g., monoclinic or tetragonal) of $BiVO_4$.

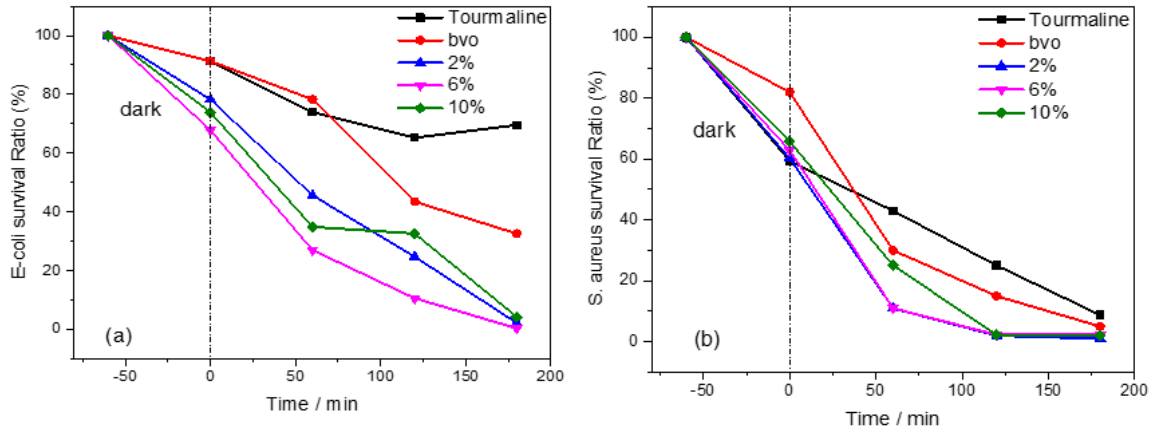

Figure 5. The antibacterial property of Tourmaline, pure BVO, and *n* wt.% Tourmaline/BVO: (a) Survival curve of *E-coil*, (b) Survival curve of *S. aureus*.

To further investigate the band structure, the band gap energy (E_9) can be estimated using the Tauc formula [28]:

$$(\alpha h\nu)^n = A(h\nu - Eg) \quad (4)$$

where $h\nu$ is the photon energy (in eV), Eg is the optical band gap (eV), α is the absorption coefficient derived from the UV–Vis DRS data, A is a proportionality constant, and n is the transition type exponent. For $BiVO_4$, which undergoes a direct allowed transition, $n = 2$ [29].

The curve derived from this formula, the "*Tauc* plot", can be utilized to accurately estimate the optical band gaps. From this plot, the estimated band gap energies for pure $BiVO_4$ and the tourmaline/$BiVO_4$ composites were approximately 2.46, 2.45, 2.38, and 2.40 eV, respectively. These results reveal a slight red shift in the absorption edge with increasing tourmaline content, indicating a narrowing of the band gap. This red shift reflects improved light-harvesting in the visible region, likely due to electronic interactions at the tourmaline/$BiVO_4$ interface and an enhanced charge transfer environment. The reduction in band gap implies better utilization of solar photons, which is advantageous for enhancing photocatalytic activity under natural sunlight.

Simultaneously, the corresponding photoluminescence (PL) spectra were employed to investigate the recombination behavior of photogenerated charge carriers, offering insights into the separation efficiency and dynamics of electron–hole pairs [30]. The PL spectra of all prepared photocatalysts were measured at room temperature using an excitation wavelength of 325 nm, as shown in Figure 6. All samples exhibited a prominent emission peak centered around 570 nm, corresponding to band-edge recombination in $BiVO_4$. Generally, high PL intensity indicates rapid recombination of photogenerated electron–hole pairs, while lower intensity suggests enhanced

 doi:10.20944/preprints202510.1766.v1

separation efficiency. Among the tested samples, the 6 wt.% tourmaline/$BiVO_4$ composite exhibited the weakest PL intensity, implying significantly reduced recombination and more efficient charge carrier separation. In contrast, the 10 wt.% tourmaline/$BiVO_4$ sample displayed the highest PL intensity, likely due to excessive tourmaline content acting as recombination centers or impeding effective charge transfer pathways. These findings suggest that moderate incorporation of tourmaline, specifically at 6 wt.%, optimally facilitates interfacial charge separation, thus contributing to improved photocatalytic performance.

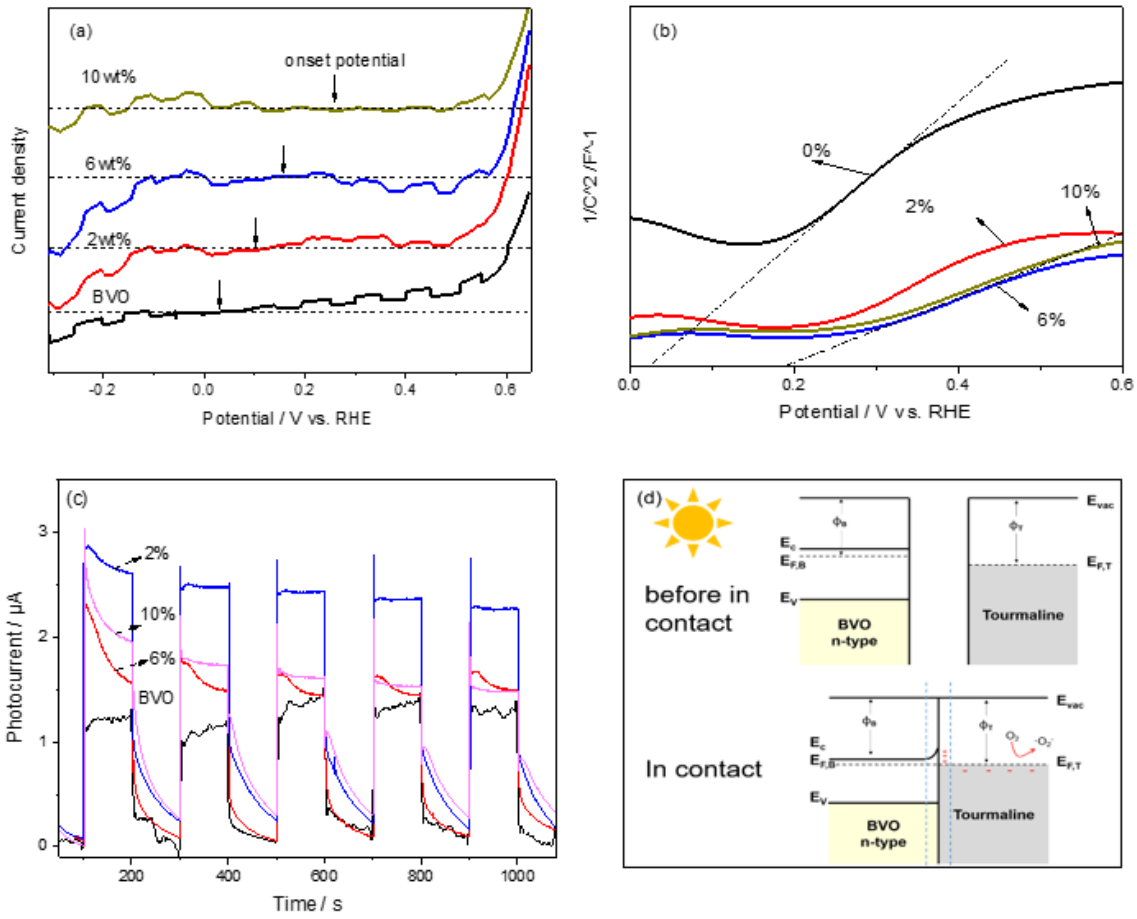

Figure 6. (a) Transient photocurrent response test, (b) M-S curve, (c) I-T curve of as-synthesized samples: Pure BVO, n wt.% Tourmaline/BVO, and (d) Schematic illustration of band structure over BVO and 2%Tourmaline/BVO.

3.3. Photocatalytic Antibacterial Efficiency

The photocatalytic properties of tourmaline/BVO compositions were evaluated by comparing their respective antibacterial abilities. The anti-microbial properties of the prepared samples were evaluated under visible light irradiation utilizing bacterial cultures of *Escherichia coli* (Gram-negative) and *Staphylococcus aureus* (Gram-positive). Both cultures were prepared at an initial concentration of 2 × 10⊚CFU/mL. Based on prior studies conducted within our group, negligible changes in bacterial count were observed in both dark and blank control conditions, confirming that visible light alone has no significant bactericidal effect in this system [31,32]. Therefore, the observed antibacterial activity can be attributed solely to the photocatalytic action of the synthesized materials.

Figure 5 presents the bacterial survival curves under visible light exposure. Notably, the 6 wt.% T/BVO composite exhibited superior antibacterial activity compared to pure $BiVO_4$, achieving nearly complete inactivation of both E. coli and S. aureus within 120 minutes. Among the two, S. aureus was more susceptible to photocatalytic inactivation, suggesting a differential response likely rooted in

 doi:10.20944/preprints202510.1766.v1

structural differences between Gram-positive and Gram-negative bacterial cell walls. Individually, both tourmaline and $BiVO_4$ demonstrated limited antibacterial activity, with tourmaline showing a slightly higher effect, consistent with previous reports. However, the significantly enhanced performance of the T/BVO composites indicates a synergistic interaction between tourmaline and $BiVO_4$, particularly at the optimized 6 wt.% loading. Photographs of the bacterial colonies post-treatment, shown in Figure S1, visually corroborate the quantitative results. The heightened antibacterial efficacy against S. aureus may be attributed to the increased interaction between the photocatalyst surface and the thick peptidoglycan layer characteristic of Gram-positive bacteria. The negatively charged surface of the polarized T/BVO composite likely promotes stronger electrostatic interactions with the bacterial cell walls, facilitating reactive oxygen species (ROS)-mediated damage.

The enhanced photocatalytic disinfection efficiency is thus proposed to arise from two main mechanisms: the electrostatic attraction between bacterial cells and the surface-polarized T/BVO composite, and the generation of reactive oxygen species, such as superoxide radicals ($\cdot O_2^-$), via surface redox reactions under visible light, leading to oxidative damage of bacterial membranes. Overall, the 6 wt.% tourmaline/$BiVO_4$ composite exhibited the most favorable photocatalytic antibacterial performance, exemplifying its potential for application in light-driven disinfection technologies and antifouling strategies in biomedical and environmental settings.

3.4. Photoelectrochemical Measurement

Photocatalytic reactions on semiconductor surfaces typically proceed through three sequential steps: (1) absorption of photons with energy equal to or greater than the semiconductor's band gap, leading to the generation of electron–hole pairs; (2) separation and migration of these photoexcited charge carriers to the surface without undergoing recombination; and (3) surface redox reactions where photogenerated electrons and holes reduce or oxidize adsorbed species, respectively. Among these, the second step (carrier separation and transport) is crucial, as it directly governs the overall photocatalytic efficiency.

To evaluate the separation and surface transfer dynamics of photogenerated carriers, photoelectrochemical (PEC) measurements were conducted. This method offers direct insight into charge transport behavior and surface reaction potential under light excitation. The photocurrent responses of the prepared thin films were measured in a 1 M Na_2SO_4 and Na_2SO_3 electrolyte under visible light illumination (390–780 nm, 100 $mW \cdot cm^{-2}$), with the films irradiated from the back side through the FTO substrate. The measured potential (vs. Ag/AgCl) was converted to the reversible hydrogen electrode (RHE) scale using the following equation:

$$E_{RHE} = E_{Ag/Agcl} + 0.059 \times pH + E^0_{Ag/Agcl} \qquad (5)$$

$$E^0_{Ag/Agcl} = 0.197V \qquad (6)$$

Figure 5a displays the photocurrent–potential (I–V) curves for the different samples under chopped light illumination. All samples exhibited increasing photocurrent densities with increasing anodic bias, a characteristic behavior of n-type semiconductors. The point at which the photocurrent switches direction, known as the onset potential, provides key information regarding the material's Fermi level (E_f) and band bending [33]. Notably, upon incorporating tourmaline, the onset potential of pristine $BiVO_4$ (0.045 V) shifted positively to 0.245 V in the composite, indicating a shift in the Fermi level and enhanced band bending, which facilitates more efficient charge separation. Furthermore, both the 2 wt.% and 6 wt.%tourmaline/$BiVO_4$ composites exhibited significantly higher photocurrent densities compared to pure $BiVO_4$, especially at higher applied potentials. This enhancement suggests improved separation and migration of photogenerated charge carriers, likely due to internal electric fields generated by the tourmaline component.

To further elucidate this behavior, Mott–Schottky (MS) plots were obtained and are shown in Figure 5b. These plots provide information about the flat-band potential and donor density, enabling

 doi:10.20944/preprints202510.1766.v1

a deeper understanding of the electrochemical properties of the materials. The corresponding equation used to interpret MS plots is as follows:

$$\frac{1}{C^2} = \frac{2}{e\varepsilon\varepsilon_0 N_D}\left(V - V_{fb} - \frac{\kappa T}{e}\right) \qquad (7)$$

Where C is the capacitance of the space charge region, e is the electron charge, ε is the dielectric constant of the semiconductor, ε_0 is the vacuum permittivity, N_D is the donor density, V is the applied potential, and V_{fb} is the flat band potential. κ is the Boltzmann constant. T is the thermodynamic temperature. The MS analysis confirms that the inclusion of tourmaline not only shifts the flat-band potential positively but also increases the carrier density, facilitating more efficient photoinduced charge transfer. These findings support the conclusion that moderate tourmaline incorporation, particularly at 6 wt.%, significantly improves the PEC performance of $BiVO_4$-based photocatalysts, offering a promising strategy for enhanced solar-driven applications.

By combining insights from the photocurrent–potential curves and Mott–Schottky (MS) plots, the direction of charge carrier movement and the underlying separation mechanism can be deduced. In pure $BiVO_4$ (BVO), upon visible light irradiation, electrons in the valence band absorb photon energy and are excited to the conduction band, generating electron–hole pairs. The resulting photovoltage (V_{photo}) facilitates the migration of these carriers toward the surface. Due to the internal electric field in the space charge region, electrons and holes are separated and migrate to different crystal facets: electrons predominantly move toward the {010} facets, while holes migrate toward the {110} facets [34]. As BVO is an n-type semiconductor, electrons are the majority carriers, and the Fermi level (E_f) tends to shift closer to the flat-band potential. However, defects within the material act as recombination centers, limiting the number of electrons that can participate in surface redox reactions. The band bending gradually decreases until the generation rate of charge carriers is balanced by the recombination rate [10].

4. Discussion

The introduction of tourmaline into the $BiVO_4$ matrix significantly enhances charge separation efficiency, leading to improved photocatalytic and antibacterial performance. Tourmaline is a naturally polar mineral with spontaneous surface polarization, even at room temperature. When an external electric field is applied or under illumination-induced internal electric fields, tourmaline generates localized surface charges that replicate the function of a semiconductor heterojunction, which promotes charge carrier separation.

Figure 5d schematically illustrates the interfacial electron transfer between tourmaline and $BiVO_4$. This transfer is primarily driven by the difference in work functions: the work function of tourmaline (ϕ_T) is higher than that of $BiVO_4$ (ϕ_B). As a result, electrons transfer from $BiVO_4$ to tourmaline until the Fermi levels of both materials equilibrate. This leads to downward band bending in $BiVO_4$ at the interface, forming a built-in electric field that further assists in electron migration. At equilibrium, a Helmholtz double layer forms at the tourmaline/BVO interface. Due to electrostatic induction, tourmaline surfaces become negatively charged while the adjacent $BiVO_4$ surface becomes positively charged. This interfacial field, combined with tourmaline's intrinsic spontaneous polarization, drives the spatial separation of electrons and holes to opposite ends of the composite structure. Electrons accumulate on one side and reduce molecular oxygen (O_2) to superoxide radicals ($^{\bullet}O_2^-$), a reactive oxygen species responsible for the enhanced antibacterial activity of the composite. Photocurrent density measurements, shown in Figure 5(c), corroborate these findings. All samples exhibited minimal current in the dark, confirming that the observed current arises from photoexcitation. Upon illumination, the photocurrent response increased significantly. Principally, the 6 wt.% tourmaline/BVO composite achieved a photocurrent density nearly double that of pristine BVO, indicating a substantial improvement in photogenerated carrier density and separation efficiency due to tourmaline incorporation.

5. Conclusions

 doi:10.20944/preprints202510.1766.v1

This study demonstrates a rational and effective strategy for enhancing the photocatalytic antibacterial performance of $BiVO_4$ by coupling it with piezoelectric tourmaline. Leveraging the intrinsic spontaneous polarization of tourmaline, the composite introduces an internal electric field that synergistically aligns with the semiconductor's band structure. This built-in field significantly promotes the separation and directional migration of photogenerated electron–hole pairs, as evidenced by reduced photoluminescence intensity, extended carrier lifetimes, and enhanced photocurrent responses. Under visible light irradiation, the tourmaline/$BiVO_4$ composite achieved bacterial inactivation rates of 96.3% for E. coli and 94.7% for S. aureus within 60 minutes—substantially outperforming pristine $BiVO_4$, which exhibited rates of 68.1% and 62.4%, respectively. These results confirm the critical role of tourmaline in facilitating charge separation and enhancing photocatalytic efficiency. The findings provide valuable mechanistic insight into the electric field–engineered photocatalytic systems and highlight the potential of piezoelectric–semiconductor composites in environmental and biomedical applications. This approach offers a promising pathway for the design of next-generation photocatalysts with superior antibacterial performance, with potential applications in water purification, environmental disinfection, and antimicrobial surface coatings.

Declaration of Competing Interest: The authors declare that they have no known competing financial interests or personal relationships that could have appeared to influence the work reported in this paper.

Supplementary Materials: The following supporting information can be downloaded at the website of this paper posted on Preprints.org. The following supporting information can be found in Figure S1: The antibacterial property of Tourmaline, pure BVO, and *n* wt.% Tourmaline/BVO: Photographs of *E-coil* colonies (c); Survival curve of *S. aureus*. (d).

Author Contributions: All authors have made equal contributions to the paper, with the main contributions as follows: "Conceptualization, J. Yu. and Fengkai Yu; methodology, Fengkai Yu; validation, Yue Yu, Alison Wang and Jia Geng; formal analysis, Nina Zhan, Alison Wang and Jia Geng; investigation, Fengkai Yu; resources, Nina Zhan, Peter Jiang, Yue Yu and Jia Geng; writing—original draft preparation, Nina Zhan and Peter Jiang; writing—review and editing, Nina Zhan, Alison Wang, Jia Geng and Peter Jiang; supervision, Jianqiang Yu; project administration, Jianqiang Yu; funding acquisition, Jianqiang Yu. All authors have read and agreed to the published version of the manuscript."

Funding: This research was funded by "The Natural Science Foundation of Shandong Province, China (ZR2019BB044)" and "The National Natural Science Foundation of China (21706140, 21976182)".

Acknowledgments: The authors have reviewed and edited the output and take full responsibility for the content of this publication.".

Conflicts of Interest: The authors declare no conflicts of interest.

References

1. F. Ramírez-Castillo, S. Loera-Muro, A. Jacques, L. Torres, D. Ponce de León, A. Escamilla-García, E. Martínez-Saldaña, Waterborne pathogens: Detection methods and challenges, *Pathogens* **2015**, *4*, pp. 307–334.
2. M. Al-Abri, C. Al-Ghafri, L. Bora, N. Dores, G. Schippers, H. Vrouwenvelder, Chlorination disadvantages and alternative routes for biofouling control in reverse osmosis desalination, *Clean Water* **2019**, *2*, pp. 1–16.
3. P. Dubey, A. Singh, O. Yousuf, Ozonation: an evolving disinfectant technology for the food industry, *Food Bioprocess Technol.* **2022**, *15*, pp. 2102–2113.
4. J. L. Sandoval, A. Friedlaender, A. Addeo, G.J. Weiss, Payments to key opinion leader physicians and drug sales of top pharmaceutical companies during the COVID-19 pandemic, *medRxiv*., 2022.

 doi:10.20944/preprints202510.1766.v1

5. S.S. Rameshwar, B. Sivaprakash, N. Rajamohan, B.A. Mohamed, D.-V.N. Vo, Remediation of tetracycline pollution using MXene and nano-zero-valent iron materials: a review, *Environ. Chem. Lett.* **2023**, *21(5)*, pp. 2995-3022.
6. S. Lu, L. Liu, Q. Yang, H. Demissie, R. Jiao, G. An, D. Wang, Removal characteristics and mechanism of microplastics and tetracycline composite pollutants by coagulation process, *Science of The Total Environment* **2021**, *786*, pp. 147508-147518.
7. P. Lian, A. Qin, Z. Liu, H. Ma, L. Liao, K. Zhang, N. Li, Facile Synthesis to Porous TiO_2 Nanostructures at Low Temperature for Efficient Visible-Light Degradation of Tetracycline, *Nanomaterials* **2024**, *14(11)*, pp. 943-961.
8. K. Han, G. H. Dong, I. Saeed, T. T. Dong, C. Y. Xiao, Morphology and photocatalytic tetracycline degradation of g-C_3N_4 optimized by the coal gangue, Chinese J Struc Chem **2024**, *43(2)*, pp. 100208-100213.
9. S. Bettini, R. Pagano, D. Valli, C. Ingrosso, M. Roeffaers, J. Hofkens, G. Giancane, L. Valli, ZnO nanostructures based piezo-photocatalytic degradation enhancement of steroid hormones, *Surf Interfaces* **2023**, *36*, pp. 102581-102599.
10. R. Tang, D. Gong, Y. Zhou, Y. Deng, C. Feng, S. Xiong, Y. Huang, G. Peng, L. Li, Unique g-C_3N_4/PDI-g-C_3N_4 homojunction with synergistic piezo-photocatalytic effect for aquatic contaminant control and H_2O_2 generation under visible light, Appl. Catal. B-*Environ.* **2022**, *303*, pp. 120929.
11. D. Dong, K. Wang, M. Yi, Y. Liang, Y. Muhammad, E. Wei, Y. Wei, T. Fujita, Preparation of TiO_2 photocatalyst microspheres by geopolymer technology for the degradation of tetracycline, *J Clean Prod* **2022**, *339*, pp. 130734.
12. S. Phanichphant, A. Nakaruk, K. Chansaenpak, and D. Channei, "Evaluating the photocatalytic efficiency of the $BiVO_4$/rGO photocatalyst," *Scientific Reports*, **2019**, *vol. 9 (1)*, pp. 16091-16099.
13. Z. Yao, H. Sun, S. Xiao, Y. Hu, X. Liu, Y. Zhang, Synergetic piezo-photocatalytic effect in a Bi_2MoO_6/BiOBr composite for decomposing organic pollutants, *Appl. Surf. Sci.* **2021**, *560*, pp. 150037.
14. G. S. Kamble et al., "$BiVO_4$ as a sustainable and emerging photocatalyst: Synthesis methodologies, engineering properties, and its volatile organic compounds degradation efficiency," *Nanomaterials*, **2023**, *13(9)*, pp. 1528.
15. L. Zhao, W. Fang, X. Meng, L. Wang, H. Bai, C. Li, In-situ synthesis of metal Bi to improve the stability of oxygen vacancies and enhance the photocatalytic activity of $Bi_4O_5Br_2$ in H_2 evolution, *J. Alloys. Compd.* **2022,** *910*, pp. 164883.
16. Z. H. Wu, J. Shen, N. Ma, Z.F. Li, M. Wu, D.F. Xu, S.Y. Zhang, W.H. Feng, Y.F. Zhu, $Bi_4O_5Br_2$ nanosheets with vertical aligned facets for efficient visible-light-driven photodegradation of BPA, Appl. Catal. B-*Environ*. **2021**, *286*, pp. 119937.
17. M. Al-Abri et al., "Chlorination disadvantages and alternative routes for biofouling control in reverse osmosis desalination," *npj Clean Water* **2019**, *2(1)*, pp. 1–16.
18. Z. Jiang, X. Tan, J. Xu, Y. Huang, Piezoelectric-Induced Internal Electric Field in Bi_2WO_6 Nanoplates for Boosting the Photocatalytic Degradation of Organic Pollutants, *ACS Appl. Nano Mater* **2022**, *5(5)*, pp. 7588-7597.
19. S. Li, C. Deng, P.G. Karmaker, K. Yang, J. Wang, W. Liu, X. Yang, Yb-doped BiOBr for highly efficient photocatalytic degradation of tetracycline hydrochloride under visible light irradiation, *Mater Res Bull* **2024**, *178*, pp. 112895.
20. X. Qian, Y. Ma, X. Xia, J. Xia, J. Ye, G. He, H. Chen, Recent progress on $Bi_4O_5Br_2$-based photocatalysts for environmental remediation and energy conversion, *Catal Sci Technol* **2024**, *14(5)*, pp. 1085-1104.
21. J.-Y. Yue, Z.-X. Pan, P. Yang, B. Tang, $Bi_4O_5Br_2$/COF S-Scheme Heterojunctions for Boosting H_2O_2 Photoproduction under Air and Pure Water, *ACS Materials Lett.* **2024,** *6(9)*, pp. 3932-3940.
22. M. Zhang, X. Sun, C. Wang, Y. Wang, Z. Tan, J. Li, B. Xi, Photocatalytic degradation of rhodamine B using $Bi_4O_5Br_2$-doped ZSM-5, *MATER CHEM PHYS* **2022,** *278*, pp. 125697.
23. X. Jin, J. Cao, H. Wang, C. Lv, H. Xie, F. Su, X. Li, R. Sun, S. Shi, M. Dang, L. Ye, Realizing improved CO_2 photoreduction in Z-scheme $Bi_4O_5Br_2$/AgBr heterostructure, *Appl. Surf. Sci.* **2022**, *598*, pp. 153758.

24. D. Liu, J. Hua, W. Zhang, K. Wei, S. Song, Q. Wang, Z. Song, H. Han, C. Ma, S. Feng, Efficient photocatalytic CO_2 reduction achieved by constructing $Bi_4O_5Br_2$/Bi-MOF Z-scheme heterojunction, *COLLOID SURFACE A* **2024**, *695*, pp. 134101.
25. H. Wang, Z. Chen, Y. Shang, C. Lv, X. Zhang, F. Li, Q. Huang, X. Liu, W. Liu, L. Zhao, L. Ye, H. Xie, X. Jin, Boosting Carrier Separation on a BiOBr/$Bi_4O_5Br_2$ Direct Z-Scheme Heterojunction for Superior Photocatalytic Nitrogen Fixation, *ACS Catal.* 2024, *14(8)*, pp. 5779-5787.
26. Y. Li, D. Han, Z. Wang, F. Gu, Double-Solvent-Induced Derivatization of Bi-MOF to Vacancy-Rich $Bi_4O_5Br_2$: Toward Efficient Photocatalytic Degradation of Ciprofloxacin in Water and HCHO Gas, *Acs Appl Mater Inter*, **2024**, *16(6)*, pp. 7080-7096.
27. X. Cong, A. Li, F. Guo, H. Qin, X. Zhang, W. Wang, W. Xu, Construction of CdS@g–C_3N_4 heterojunction photocatalyst for highly efficient degradation of gaseous toluene, STOTEN **2024**, *913*, pp. 169777.
28. L. Yuan, B. Weng, J.C. Colmenares, Y. Sun, Y.J. Xu, Multichannel Charge Transfer and Mechanistic Insight in Metal Decorated 2D–2D Bi_2WO_6–TiO_2 Cascade with Enhanced Photocatalytic Performance, *Small*, **2017**, *13(48)*, pp. 1702253.
29. X. Meng, S. Wang, C. Zhang, C. Dong, R. Li, B. Li, Q. Wang, Y. Ding, Boosting Hydrogen Evolution Performance of a CdS-Based Photocatalyst: In Situ Transition from Type I to Type II Heterojunction during Photocatalysis, *ACS Catal.* **2022,** *12(16)*, pp. 10115-10126.
30. G. Zhu, S. Li, J. Gao, F. Zhang, C. Liu, Q. Wang, M. Hojamberdiev, Constructing a 2D/2D $Bi_2O_2CO_3$/$Bi_4O_5Br_2$ heterostructure as a direct Z-scheme photocatalyst with enhanced photocatalytic activity for NOx removal, *Appl. Surf. Sci.* **2019**, *493*, pp. 913-925.
31. Q. Pan, J. Wang, H. Chen, P. Yin, Q. Cheng, Z. Xiao, Y.-z. Zhao, H.-B. Liu, Piezo-photocatalysis of Sr-doped $Bi_4O_5Br_2$/Bi_2MoO_6 composite nanofibers to simultaneously remove inorganic and organic contaminants, *J Water Process Eng* **2023,** *56*, pp. 104330.
32. T. Ma, C. Yang, L. Guo, R.A. Soomro, D. Wang, B. Xu, F. Fu, Refining electronic properties of Bi_2MoO_6 by In-doping for boosting overall nitrogen fixation via relay catalysis, *Appl. Catal. B-Environ.* **2023,** *330*, pp. 122643.
33. H. Huang, L. Liu, Y. Zhang, N. Tian, One pot hydrothermal synthesis of a novel $BiIO_4$/Bi_2MoO_6 heterojunction photocatalyst with enhanced visible-light-driven photocatalytic activity for rhodamine B degradation and photocurrent generation, *J. Alloys. Compd.* **2015**, *619*, pp. 807-811.
34. J. Fan, L. Shi, H. Ge, J. Liu, X. Deng, Z. Li, Q. Liang, Regulating the Oxygen Vacancy on Bi_2MoO_6/Co_3O_4 Core-Shell Nanocage Enables Highly Selective CO_2 Photoreduction to CH_4, *Adv. Funct. Mater.* **2024,** *35(1)*, pp. 2412078.